Journal of Controlled Release 397 (2026) 115128

Contents lists available at ScienceDirect

Journal of Controlled Release

journal homepage: www.elsevier.com/locate/jconrel

Muscle contribution in lipid nanoparticle mediated mRNA vaccine delivery and efficacy

Mathieu Repellin [a], Stefano Ugel [b], Francesco De Sanctis [b], Laurent Coudert [c,d], Tian Wang [b], Cristina Anselmi [b], Valentina Andretto [a], Isabella Scionti [c], Joris Dimastromatteo [a], Jacqueline Sidi-Boumedine [e,f], Julien Carras [c,d], Pierre-Yves Dugas [g], Fabrice Brunel [g], Manuela Malatesta [h], David Kryza [a], Laurent Schaeffer [c,d,1], Arnaud Jacquier [c,d,1], Giovanna Lollo [a,i,*]

[a] Université Claude Bernard Lyon 1, University of Lyon, CNRS, LAGEPP UMR 5007, 69100 Villeurbanne, France
[b] Department of Medicine, Section of Immunology, University of Verona, 37129 Verona, Italy
[c] Université Claude Bernard Lyon 1, Institut NeuroMyogène, University of Lyon, CNRS UMR 5310, INSERM U1217, 69008 Lyon, France
[d] Hospices civils de Lyon, Centre de Biotechnologie Cellulaire, University of Lyon, groupement hospitalier Est, Bron, France
[e] Hospices Civils de Lyon, Department of Medical Oncology, Lyon, France
[f] Gastroenterology and technologies for health, Research unit INSERM UMR 1052 CNRS UMR 5286, Cancer Research Center of Lyon, France
[g] Université Claude Bernard Lyon 1, University of Lyon, CNRS, CP2M UMR 5128, 69100 Villeurbanne, France.
[h] Department of Neurosciences, Biomedicine and Movement Sciences, Anatomy and Histology Section, University of Verona, 37134 Verona, Italy
[i] Institut universitaire de France (IUF), Paris, France

ARTICLE INFO

Keywords:
Nanomedicine
mRNA vaccines
Skeletal muscle
Biological barriers
Immunity

ABSTRACT

The remarkable success of mRNA-lipid nanoparticles (LNP) vaccines during the SARS-CoV-2 pandemic have highlighted the critical role of this cutting-edge technology as a cornerstone for contemporary vaccine innovation. Efforts to enhance mRNA-LNP vaccine efficacy have driven specific interest in optimizing nanoparticle design to improve immune cell transfection. Nevertheless, the precise mechanisms driving immune responses, including cell identity and their activation states within immune and local tissues, remain unclear and system-dependent. Muscle tissue is an ideal site for mRNA vaccine administration due to its ribosome abundance, ensuring efficient translation of the delivered mRNA into the encoded protein. Additionally, the localized nature of muscle injections ensures controlled biodistribution and minimizes systemic side effects, making it a safe and effective route for generating robust immune responses. In line with these observations, we developed a lipid-polymer hybrid nanosystem that effectively complexes mRNA, demonstrating high efficiency in transfecting muscle cells and tissue. Importantly, this delivery resulted in a robust adaptive immune response, characterized by both potent humoral and cellular immunity, highlighting the effectiveness of this nanosystem for mRNA-based vaccination. Overall, these findings highlight the need to consider the role of muscle cells as potential antigen-producing reservoirs in immune modulation when designing mRNA vaccines.

1. Introduction

Recent breakthroughs in developing lipid nanoparticles (LNP) have revolutionized nucleic acid delivery, unlocking new frontiers in gene therapy and holding great promise for treating a wide range of diseases. Over the last decade, this technology gained great interest from groundbreaking research to cutting-edge therapeutics, as highlighted with the first commercially approved small interfering RNA-LNP therapy, Onpattro®, for treating hereditary transthyretin amyloidosis [1]. LNP have also proven their worth in delivering messenger RNA (mRNA), notably with the successful deployment of the Spikevax® and Comirnaty® vaccines against SARS-CoV-2 during the COVID-19 global health crisis [2,3]. Following this success, numerous clinical trials are currently underway to explore the broad potential of mRNA-LNP to

* Corresponding author.
E-mail address: giovanna.lollo@univ-lyon1.fr (G. Lollo).
[1] These authors equally contributed to this work.

https://doi.org/10.1016/j.jconrel.2026.115128
Received 18 November 2025; Received in revised form 13 June 2026; Accepted 23 June 2026
Available online 30 June 2026

protect against various diseases and infections [4–6].

Intramuscular (i.m.) injection is the primary route for vaccine delivery. This administration route is strategically significant because muscle tissue provides a unique cellular environment, primarily consisting of myofibers, as well as endothelial cells, immune cells, fibroblasts, muscle stem cells and Schwann cells [7,8]. Muscle tissue's extensive vascular network allows for efficient uptake and widespread distribution of antigens, while the presence of antigen-presenting cells (APCs), such as dendritic cells (DCs) and macrophages, is crucial for triggering an effective immune response.

Elucidating the delivery pathways and immune mechanisms activated by mRNA-LNP administration is critical for advancing the design of safer, more effective mRNA vaccines. Nevertheless, the precise vaccine trafficking and the specific cell types engaged remain challenging to explore and are still ambiguous. The initial studies focused on optimizing mRNA-LNP to target and enhance direct transfection efficiency in APCs, considered as the coveted milestone for initiating the adaptive immunity by priming naïve T cells [9–11]. However, few recent studies have detailed the potential benefit of also transfecting local myofibers [12,13]. Indeed, muscle cells are highly efficient protein-producing cells and may have an underestimated role in enhancing local immune activation by expressing vaccine-induced antigens and releasing cytokines and chemokines able to recruit and activate APCs [12,14]. Additionally, they facilitate cross-talk with γδ T cells and are involved in favoring Th1 and polyfunctional $CD8^+$ T cell responses [14–16]. Elucidating the relationship between mRNA-loaded nanoparticles and myocytes, including cellular uptake and transfection efficiency, could provide key insights for optimizing mRNA-based vaccines.

To address this question, we previously developed an innovative composition of hybrid lipid-polymer nanoparticles (hLNP), entirely free of cholesterol and PEG, that enables highly efficient nucleic acid delivery [17,18]. Conventional LNPs are generally composed of four key components: an ionizable lipid, a phospholipid, cholesterol, and a polyethylene glycol (PEG)-lipid. This relatively fixed formulation contributes to consistent physicochemical properties but also to a persistent liver tropism following systemic administration. They have been shown to trigger pro-inflammatory immune responses which may adversely affect their therapeutic efficacy [19]. Notably, the presence of cholesterol and PEG derived lipids in LNPs affects both immune response and liver tropism both after intravenous or local administration. It has been demonstrated that decreasing the cholesterol content in mRNA-LNPs suppressed protein expression in the liver during intramuscular administration [20].

Here, we optimized a novel LNP formulation by modulating its composition through microfluidic production and established conditions enabling efficient freeze-drying to improve long-term stability and facilitate storage. In parallel, we performed an extensive physicochemical characterization, including small-angle X-ray scattering (SAXS), to elucidate the structural organization of our mRNA-hLNPs. Then, we conducted an in-depth *in vitro* investigation to better understand the delivery pathway of our mRNA-loaded hLNP, while testing their overall efficacy in promoting immunomodulation. After providing stable hLNP enabling efficient mRNA association, their ability to transfect muscle cells has been tested *in vitro* on mouse muscle cell lines and *ex vivo* on explanted murine muscle fibers. Subsequently, the tissue biodistribution, protein expression, and cell subsets engaged have been investigated *in vivo* following the i.m. administration of the lead candidate in a reporter mouse model. Finally, their ability to trigger both cellular and humoral immune responses has been explored *in vivo* to further support the significant involvement of myocytes in the delivery path of our nanosystem.

2. Materials and methods

2.1. Materials

18:1 TAP (DOTAP), 18:1 (Δ9-Cis) PE (DOPE), ALC-0315, DSPC, Cholesterol, ALC-0159, 18:1 Cyanine 5 PE and 18:1 Liss Rhod PE were purchased from Avanti Research (Merck, Saint-Quentin-Fallavier, France). Coatsome SS-M was obtained from NOF Corporation (Tokyo, Japan). Sodium hyaluronate 40 K was purchased from Lifecore Biomedical (Minnesota, USA). N1-mψ mRNA-eGFP, N1-mψ mRNA-Cre and N1-mψ mRNA-OVA were obtained from OZ Biosciences (Marseille, France). EZ Cap Cy5-eGFP-mRNA (5moUTP) was obtained from Tebubio (Le Perray-en-Yvelines, France). Sybr® Green II, LIVE/DEAD™, Phalloidin-Atto 488, DAPI, Fluoromount-G, GFP Polyclonal Antibody-Alexa Fluor™ 488, CD11c Monoclonal Antibody (N418), Goat anti-Armenian Hamster-Alexa Fluor™ 488, CD3e Monoclonal Antibody (145-2C11), CD28 Monoclonal Antibody (37.51), CD3 Monoclonal Antibody (17A2)-Brilliant Violet™ 421, CD4 Monoclonal Antibody (GK1.5)-PE-Cyanine7, CD11b Monoclonal Antibody (M1/70)-FITC, IFN gamma Monoclonal Antibody (XMG1.2)-PE, Donkey anti-Rabbit, Alexa Fluor™ 488 and Brefeldin A Solution were purchased from Invitrogen (ThermoFischer Scientific, Illkirch, France). Trehalose, Mannitol, N-butyldiethanolamine, Antipyrine, Ovalbumin protein and Anti-Laminin (LAMA1) Antibody were obtained from Sigma-Aldrich (Saint-Quentin-Fallavier, France). *N*-methylnicotinamide was purchased from Tokyo Chemical Industry (Zwijndrecht, Belgium). Quant-iT™ RiboGreen, collagenase type II and NBT/BCIP Substrate Solution was obtained from ThermoFischer Scientific (Illkirch, France). Purified anti-mouse CD64 Antibody was purchased from BioLegend (Amsterdam, The Netherlands). Rat Anti-Mouse IFN-γ (R4–6A2), Biotin Rat Anti-Mouse IFN-γ (XMG1.2), AKP Streptavidin and Rat Anti-Mouse CD8a (53–6.7) APC-Cy7 were obtained from BD Pharmingen (New Jersey, USA). CD40-specific mAb was purchased from BioXcell (Lebanon, USA). Goat anti-mouse IgG (H + L) secondary antibody with HRP was obtained from GeHealthcare (Milan, Italy).

2.2. mRNA-hLNP production

hLNP were produced by microfluidic mixing. Briefly, an ethanol phase containing DOTAP, DOPE and Coatsome SS-M (molar ratio 50:25:25) was mixed with an aqueous phase (HEPES, 100 mM, pH 5.5) at a flow rate ratio of 1:3 and a total flow rate of 15 mL/min. hLNP were dialyzed against the same aqueous phase to eliminate ethanol in a 10 kDa molecular weight cut-off slide-a-lyzer (Slide-A-Lyzer™ MINI, 10 kDa, Thermo-Fischer Scientific) for 4 h and stored at 4 °C. Fluorescently-labelled hLNP were obtained using the same process by incorporating Cy5- or Rhodamine-labelled PE in the ethanol phase (2 mol% of total lipids). mRNA-hLNP were then obtained by gentle pipette-mixing hLNP and the mRNA of interest at varying nitrogen-to-phosphate (N/P) ratios. Subsequently, mRNA-hLNP complexes were coated with sodium hyaluronate 40 kDa at a 1:1 mass ratio (HA:lipids) by gentle pipette-mixing at a 1:2 volume ratio (HA:mRNA-hLNP). Benchmark mRNA-LNPs were produced by microfluidic, mixing an ethanol phase containing ALC-0315, DSPC, Cholesterol, ALC-0159 (molar ratio 46.3:9.4:42.7:1.6) with an aqueous phase (sodium acetate 25 mM pH 4.5) at a flow rate ratio of 1:3 and a total flow rate of 12 mL/min. ALC-based benchmark mRNA-LNPs were then dialyzed as previously described against PBS pH 7.4.

2.3. Physicochemical and morphological characterization of mRNA-hLNP

The hydrodynamic diameter, PDI and zeta potential were measured using a Malvern Zetasizer® Nano ZS (Malvern Instruments, Worcestershire, UK). mRNA encapsulation efficiency was determined using RiboGreen assays (Quant-iT™ RiboGreen) according to the

manufacturer's protocol and imaging was performed using Spark® microplate reader (TECAN). mRNA complexation efficiency was also determined using Sybr Green II® gel agarose electrophoresis. Samples containing 0.2 μg mRNA were loaded onto 1% (*w*/w) agarose gel and migrated for 30 min at 80 V, while parallel samples were incubated with 0.1% Triton X-100 prior to loading to disrupt the nanoparticle structure and release the complexed mRNA as a control. Imaging was performed using the Gel Doc™ EZ imager (Bio-Rad).

The morphology of hLNP and mRNA-hLNP was investigated by cryogenic transmission electron microscopy (cryo-TEM). Briefly, 3 μL were deposited onto a 300-mesh Lacey carbon film grid and quench-frozen in liquid ethane to produce protective vitreous ice (Thermo-Fischer, FEI Vitrobot Mark IV). Cryo-TEM imaging was performed using JEOL 1400F cryo-electron microscope - 120 kV LaB6 (Centre Technologique des Microstructures (CTμ), Université Claude Bernard Lyon 1, Villeurbanne) equipped with a Gatan Rio16 camera used in low-dose conditions.

2.4. Small-Angle X-ray Scattering (SAXS)

SAXS measurements were performed at the ID02 beamline of the European Synchrotron Radiation Facility (Grenoble, France). Experiments were carried out at an energy of 12.2 keV with a sample-to-detector distance of 100 cm, using a Eiger2-4 M camera. The recorded images were corrected from dark current and flat field and normalized with respect to the intensity of the incident beam. The azimutal integration of the corrected images gave the radial integration (scattering curves). Finally, the obtained scattering curves were calibrated (q-axis) using silver behenate and corrected for sample transmission and background subtraction. SAXS were analyzed using SASfit.0.93.11 software. The form-factor equations used to fit the curves are given below for the different situations.

Guinier's approximation states that at low-q the scattering profile can be approximated as follows:

$$I(q) = I(0)e^{-\frac{q^2R_g^2}{3}}$$

where Rg is the radius of gyration and I(0) is the intensity at zero scattering angle (q = 0).

The repeat distance of the multilamellar lipid structure, d, was determined from the position of the Bragg peak (d = 2π/q). The Bragg peaks were fitted using Voigt profile. The Voigt peak model is widely used for peak fitting in X-ray scattering, spectroscopy, and diffraction data analysis. It is a convolution of a Gaussian function (representing instrumental broadening) and a Lorentzian function (representing intrinsic broadening). The amplitude version of the Voigt peak is parameterized as:

$$I(q) = A\frac{\int_{-\infty}^{\infty}\frac{\exp\left(-u^2\right)}{\frac{\gamma^2}{2\sigma^2}+\left(\frac{q-q_{max}}{\sqrt{2}\sigma}-u\right)^2}du}{\int_{-\infty}^{\infty}\frac{\exp(-u^2)}{\frac{\gamma^2}{2\sigma^2}+u^2}du}$$

With A the amplitude of the Voigt peak q max the center of the peak, σ width of Doppler (Gaussian) contribution (fixed value, σ = 0.001) and γ the width of Lorentzian contribution.

2.5. Freeze-drying process of mRNA-hLNP

For freeze-drying process, mRNA-hLNP formulations were diluted to obtain a final concentration of 1.5% Trehalose and 5% Mannitol. Freeze-drying procedure was carried out in a Cryonext pilot freeze-dryer (Cryonext, Saint-Aunès, France). The freeze-drying technology was as follows: freezing at −45 °C for 4 h in the freeze-dryer chamber; primary drying at −35 °C for 10 h and then to 0 °C for 5 h (0.25 mBar); secondary drying at 4 °C for 5 h (0.1 mBar). Finally, vials were sealed and stored at 4 °C for 4 months before analysis. Samples were reconstituted in an equal volume of ultra-pure water as used prior to the freeze-drying process.

2.6. Cell culture and transfection efficiency

C2C12 myoblasts (ATCC® CRL-1772) were cultured under humidified atmosphere with 5% CO_2 at 37 °C using DMEM, supplemented with 10% (*v*/v) FBS, 100 units/mL of Penicillin-Streptomycin. To induce differentiation into myotubes, the myogenic induction medium was replaced with myogenic differentiation medium composed of DMEM GlutaMax, supplemented with 1% (v/v) fetal horse serum (FHS) and 100 units/mL of Penicillin-Streptomycin for 6 days. For this experiment, mRNA encoding for enhanced green fluorescent protein (eGFP) was employed in this experiment as a reporter tool. For transfection efficiency, myoblasts were seeded at 10,000 cells/cm^2 in 24-well plates. After overnight recovery, the cells were treated with mRNA(eGFP)-hLNP at desired concentrations for 2 h and then received fresh media. After 24 h incubation time, cells were detached with trypsin and cell supernatant media and detached cells were combined and stained with LIVE/DEAD™ solution. Data were acquired with BD LSR 2 flow cytometer and analyzed using FlowJo software. Regarding myotubes, cells were seeded at 30.000 cells/cm^2 onto 4-comportements Lab-tek culture chambers. After myogenic differentiation, myotubes were treated at the desired concentrations for 2 h and fixed in 4% paraformaldehyde (PFA) after 24 h incubation time. Samples were mounted in Fluoromount-G and imaged with a Leica DM400B using a 40× objective. For each sample, 100 myotubes were manually counted for GFP expression. Viromer mRNA (Lipocalyx®) was used as *in vitro* commercial agent according to the manufacturer's instructions.

2.7. In vitro internalization study

C2C12 cells were seeded onto 4-comportements Labtek culture chamber as previously described. The cells were then treated for 30 min, 2 h and 24 h with 1 μg of eGFP-mRNA labelled with Cy5 complexed to Rhodamine-labelled hLNP. The samples were then fixed with 4% PFA and stained with Phalloidin-Atto 488 (1:500) and DAPI (stock 20 mM; 1:10000) for 1 h at room temperature. The samples were finally mounted in Fluoromount-G and imaged with a Zeiss LSM880 confocal laser scanning microscope (Carl Zeiss AG, Oberkochen, Germany) using a 63× objective.

2.8. Ex vivo internalization and transfection investigations

Muscle fibers were explanted from healthy C56Bl/6 mice sacrificed in a separate study as control mice. Briefly, Extensor Digitorum Longus muscles were carefully isolated and digestion was performed in DMEM containing 600 U/mL of collagenase type II solution at 37 °C for 75 min to liberate individual myofibers. Following enzymatic digestion and separation, the myofibers were dissociated by gentle trituration with a glass pipette and around 30-fibers were plated by petri dish. The myofibers were then cultured under humidified atmosphere with 5% CO_2 at 37 °C in DMEM containing 20% FBS and 5 ng/mL bFGF and treated with 5 μg of mRNA-eGFP complexed to Rhodamine-labelled hLNP for 2, 24 and 72 h. The samples were then fixed with 4% PFA, stained with GFP antibody (1:200) and DAPI (stock 20 mM; 1:10000) for 1 h at room temperature and finally mounted in Fluoromount-G. Imaging was performed with a Zeiss LSM880 as previously described.

2.9. Animals

For Ai9-Rosa TdTomato mouse strain (The Jackson Laboratory, #007909), animal protocols were approved by the local animal ethics committee of University Claude Bernard Lyon 1, and mice were bred according to both French and European regulations (authorization

number #41079 and #47527).

For C57BL/6 J mouse strain (Charles River Laboratories, #027), animal protocols were approved by the Italian Ministry of Health and mice were bred according to both Italian and European regulations (authorization number C46F4.26 approved by the Ministerial Decree Number 993/2020-PR of July 24, 2020 [PI: Stefano Ugel]). All animal experiments were conducted following the Amsterdam Protocol on animal protection and welfare: mice were monitored daily and euthanized when displaying excessive discomfort.

2.10. Overall in vivo biodistribution and transfection efficiency of mRNA-hLNP

The *in vivo* biodistribution and transfection efficiency study of mRNA-hLNP following intramuscular administration were conducted on Ai9 Rosa TdTomato males at 8–12 weeks of age. To this end, 5 μg of mRNA-Cre complexed to Cy5-labelled hLNP in a volume of 50 μL were injected into the left Tibialis Anterior (TA) of mice. The animals were then sacrificed by cervical dislocation under isoflurane anesthesia following 2 h, 24 h or 1-week post-administration ($N = 3$/group). For control group, mice were administered with 50 μL of 0.9% NaCl solution and sacrificed 1-week post-administration. For each administration time point, organs were collected and imaged for the presence of Cyanine 5 and TdTomato expression using a U-IO Milabs Optical Imaging System (MiLabs, Utrecht, The Netherlands).

2.11. In vivo distribution and transfection efficiency of mRNA-hLNP in myofibers

The *in vivo* distribution and transfection efficiency study of mRNA-hLNP were conducted on Ai9 Rosa TdTomato males at 8–12 weeks of age. To this end, 5 μg of Cre recombinase mRNA complexed to Cy5-labelled hLNP in a volume of 50 μL were injected into both TA of mice. Animals were then sacrificed by cervical dislocation under isoflurane anesthesia following 24 h, 72 h or 1-week post-administration ($N = 5$/group). For control group, mice were administered with 50 μL of 0.9% NaCl solution and sacrificed 1-week post-administration. One TA muscle per mouse was then isolated and: (i) fixed overnight in 4% PFA, (ii) immersed overnight in 30% saccharose PBS solution, (iii) embedded in Tissue-Tek OCT compound and frozen in isopentane cooled with liquid nitrogen. 10 μm thick muscle sections were transversally cut from frozen TA muscles using a Leica CM 3050S cryostat (Leica Biosystems, Nussloch, Germany). Muscle cross-sections were incubated overnight at 4 °C with Laminin (1:200), CD11c (1:200) or CD64 (1:200) primary antibody and then incubated 1 h at room temperature with the corresponding secondary antibody rabbit 488 or Armenian hamster 488, and with DAPI (stock 20 mM; 1:10000). Sections were finally mounted in Fluromount-G and observed with a Zeiss LSM880 microscope, using a 10× objective and performing tile scan acquisitions. The same process was also conducted on the collected spleen and inguinal lymph nodes.

The second TA muscle was processed for tissue clearing according to the CUBIC protocol [21]. Briefly, after overnight fixation in 4% PFA at 4 °C, TA muscles were incubated in CUBIC-L (10% *w*/w N-butyldiethanolamine +10% w/w Triton X-100) for 4 days at 37 °C under gentle agitation. After overnight washing in PBS with gentle agitation, muscles were immersed in a 1:1 mixture of water and CUBIC-RA (45% w/w antipyrine +30% *N*-methylnicotinamide) for 1 day at room temperature. The samples were finally incubated in CUBIC-RA for 2 days at room temperature prior imaging with a light sheet fluorescent microscope Zeiss Z1 (Carl Zeiss AG, Oberkochen, Germany) equipped with a X5 objective.

2.12. In vivo immunization

Experiments were conducted on C57BL/6 J mice at 8–10 weeks of age. For this experiment, mRNA encoding ovalbumin (OVA) was employed in this experiment as a model antigen. Mice were i.m. (quadriceps) immunized with mRNA(OVA)-hLNP at a dose of 10 μg mRNA per mouse twice using a prime-boost strategy at a 2 weeks interval.

2.13. ELISPOT assay

Vaccinated and unvaccinated mice were euthanized and the spleens were harvested fourteen days after last immunization. Single-cell suspensions of splenocytes were used for anti-IFNγ ELISPOT assay, as previously described [22]. Briefly, 10^6 splenocytes were seeded on IFNγ-precoated (BD PharMingen) 96-well MAIP plates (Millipore) and incubated at 37 °C for 20 h with 1 mg/mL of H-2Kb-restricted OVA MHC class I epitope (SIINFEKL) or I-Ad-restricted OVA MHC class II epitope (ISQAVHAAHAEINEAGR) or control H-2Kb-restricted peptide of β-galactosidase (β-gal$_{96–103}$: DAPIYTNV). CD3e monoclonal antibody and anti-CD28 were used at 5 mg/mL as a positive control. Plates were then incubated for 12 h at 4 °C with rat anti-mouse biotin-conjugated IFNγ, followed by 3 h at 25 °C with streptavidin-AKP and finally with NBT/BCIP for color development. An ELISPOT reader (AID, Germany) was used to count the spots.

2.14. Intracellular staining (ICS) for IFN-γ detection by Flow cytometry

5×10^6 mouse splenocytes isolated from vaccinated and unvaccinated mice were incubated in 1 mL RPMI with 10% FCS with the indicated peptides (final concentration of each peptide, 1 μg/mL) and 1 μg/mL brefeldin A at 37 °C for 12–16 h as previously described [23]. Cells were washed, stained with surface antibodies: Brilliant Violet 421 labelled CD3 (clone 17A2), PE-Cyanine7 labelled CD4 (clone GK1.5), APC-Cy7 labelled CD8α (clone 53–6.7), FITC labelled CD11b (clone M1/70), fixed, permeabilized, and incubated with PE-labelled IFN-γ antibody (clone XMG1.2). Cells were fixed with 1% formaldehyde solution in PBS and analyzed on a FACSCanto flow cytometer using Flowjo software (Treestar).

2.15. Enzyme-Linked Immunosorbent Assay (ELISA) for Antibody Titer

Indirect ELISA was performed to measure the antibody titer. The high-binding 96-well plates (Corning) were covered with 100 μL of ovalbumin protein (Albumin chicken egg A-5503, Sigma) with a concentration of 20 μg/mL at 4 °C overnight. The plates were then washed three times with PBS-T and blocked by 1% bovine serum albumin solution (Sigma-Aldrich). The sera collected from immunized and control mice were initially diluted starting from 1:50. Then, a twofold serial dilution was performed on all serum samples. 100 μL of samples were added to the plates for 2 h at 37 °C. Then, the plates were washed and then incubated with goat anti-mouse IgG (H + L) secondary antibody with HRP at 1:1000 for 1 h at 37 °C. Next, the plates were washed and 50 μL of TMB ELISA substrate solution was added for 15 min incubation at room temperature. Then, 50 μL of stop solution (0.16 M sulfuric acid) was added. SpectraMax ABS Reader (Miolecular Device) was used to measure the Optical Density (OD450).

2.16. Enzyme-Linked Immunosorbent Assay (ELISA) for Cytokine Quantification

Mouse serum cytokine levels were measured using ELISA kits for GM-CSF, IL-12p70, IFN-γ and IL-6 (Invitrogen). Briefly, 96-well plates precoated with capture antibodies were incubated with diluted serum samples and cytokine standards. After washing, biotinylated detection antibodies were added, followed by streptavidin-HRP and TMB substrate for colorimetric development. The reaction was stopped with stop solution, and absorbance was measured at 450 nm with background correction at 570 nm using a SpectraMax ABS Reader (Molecular

Devices).

2.17. Figure design

Schematic figures were prepared using Adobe Illustrator (illustrator.com).

3. Results

3.1. Development of an innovative lipid-based mRNA vaccine

An innovative hybrid-lipid-based nanoparticle (hLNP) composition was developed by mixing 1,2-Dioleoyl-3-trimethylammonium propane (DOTAP), 1,2-dioleoyl-sn-glycero-3-phosphoethanolamine (DOPE) and Coatsome® SS-M (schematized in Fig. 1) [17,18].

Unlike conventional LNP formulations, this original patented formulation is devoid of cholesterol and polyethylene glycol. Following the microfluidic process, the resulting tiny hLNP liposomes were characterized by a size around 15–30 nm (Fig. 2A) and a positive surface charge of around +30 mV (Fig. 2B). The same physicochemical properties were obtained for fluorescent hLNP obtained by incorporating 2% molar of Cy5- or Rhodamine-labelled PE. Following complexation with mRNA at different lipid-to-nucleic acid ratios (expressed as N/P ratio for nitrogen-to-phosphate) and subsequent coating with hyaluronic acid, all obtained nanosystems exhibited an average size in the range of 110–150 nm with a PDI between 0.12 and 0.25, values consistent with the acceptable range for mRNA-LNPs produced in this study *via* manual mixing of pre-formed LNPs with mRNA (Fig. 2A). Furthermore, low batch-to-batch variability and consistent distributions were observed across replicates ($n = 6$ independent replicates). A slight increase in the hydrodynamic size of the nanosystems was observed with higher N/P ratios. This trend may reflect the formation of more successive lipid-mRNA layers as the lipid proportion increases. All complexes displayed a surface potential of around −20 mV, reflecting the presence of the negatively charged carboxyl groups of the hyaluronic acid coating on the mRNA-hLNP (Fig. 2B). Assembly of hyaluronic acid on the surface of the mRNA-hLNP represents a promising strategy to enhance colloidal stability and reduce non-specific interactions with serum proteins while maintaining a PEG-free formulation. Moreover, hyaluronic acid can facilitate targeted uptake by muscle cells through interactions with CD44 and other HA-binding receptors expressed on myofibers [24]. RiboGreen® and electrophoretic displacement assays demonstrated efficient mRNA complexation, with encapsulation efficiencies consistently around 95% across all tested N/P ratios (Fig. 2C and D). The slight decrease in signal observed with increasing N/P ratios indicates stronger complexation at higher N/P ratios, resulting from the excess of positive charges.

Morphological analysis performed at cryo-TEM revealed the physical rearrangement from the distinct single lipid bilayers of the tiny hLNP to the characteristic multilamellar particle structures of lipoplexes after mRNA complexation, where successive layers of mRNA and lipids are intercalated (Fig. 2E, supplementary Fig. S1) [25,26]. In the absence of PEGylated components, these assemblies do not adopt perfectly spherical, individualized morphologies, which likely accounts for the observed variability in particle shape despite a conserved multilamellar internal structure. This inner architecture was further supported by structural analysis using SAXS measurements (Fig. 2F). SAXS-scattering curves demonstrated the presence of two overlapping but distinguishable Bragg peaks q = 0.96 and 1.1 nm^{-1}. The main peak (q = 1.1 nm^{-1}) typically corresponds to the characteristic periodicity of the lamellar structures in the sample. This periodicity is directly related to the repeat distance (or d-spacing) between adjacent bilayers in the vesicles which is found to be around 5.5 nm. In typical phospholipid bilayers, the thickness is usually around 3–5 nm, while the remaining ~1–2 nm can be attributed to the interlamellar water layer, which is consistent with hydrated systems [27,28]. In addition to this distinct peak, a broad peak is observed around q = 0.96 nm^{-1}, which can be attributed to less densely packed lipid membranes with an interlamellar spacing of 6.5 nm. Moreover, increasing the N/P ratio led to an increased amplitude of the Bragg peak at q = 0.96 nm^{-1} and a decrease at 1.1 nm^{-1}, indicating looser membrane packing and reduced structural order, consistent with deviation from the charge-stoichiometric ratio.

3.2. Stabilization of Lipid nanoparticles formulation via freeze-drying

The mRNA-vaccines developed for SARS-CoV-2 highlighted significant challenges related to the strict cold-chain requirements of mRNA-based vaccines, necessitating ultra-low temperatures for long-term stability that may impede global distribution and further limit accessibility for low- and middle-income countries [29]. In response to these obstacles, freeze-drying of mRNA-based vaccines represents a promising strategy to extend their shelf-life and facilitate their storage [30,31]. To this end, mRNA-hLNP (N/P ratio 1.5) were lyophilized in the presence of different concentrations of mannitol and trehalose as lyoprotectants aiming to reduce stress induced by the freeze-drying process (Fig. 3A).

Post-lyophilization, physicochemical properties were monitored after resuspension to investigate the stability and structural integrity of the mRNA-hLNP. Resuspended nanosystems freeze-dried in the single presence of trehalose resulted in non-redispersible mRNA-hLNP, with lipids fused and crushed to the bottom of the vial, highlighting the essential role of mannitol as a bulking agent (Fig. 3B). On the other hand, nanosystems lyophilized only in mannitol, which were tested later

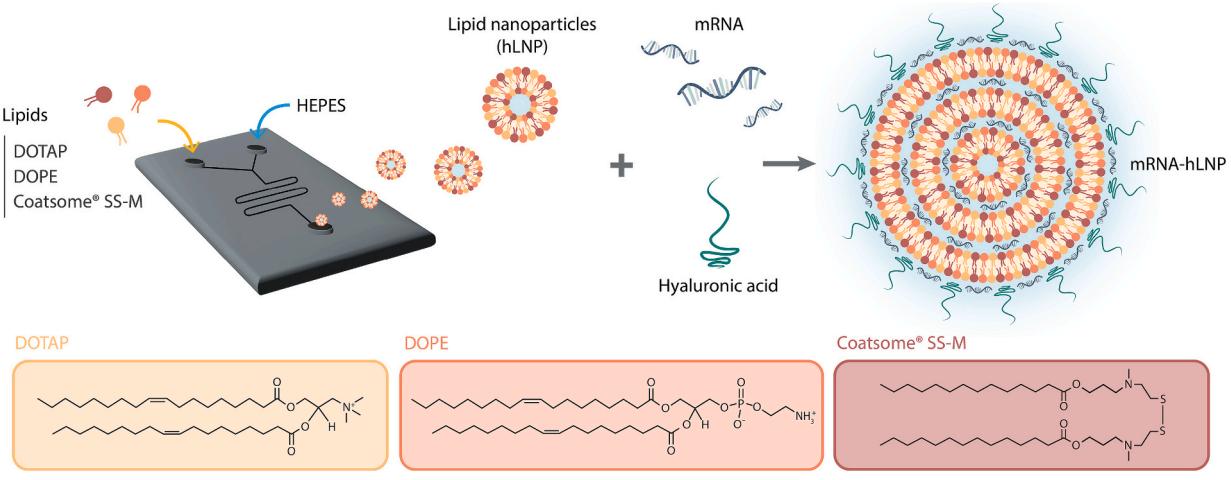

Fig. 1. Formulation process of mRNA-hLNP. Schematic representation depicting the key features of the mRNA-hLNP engineering process.

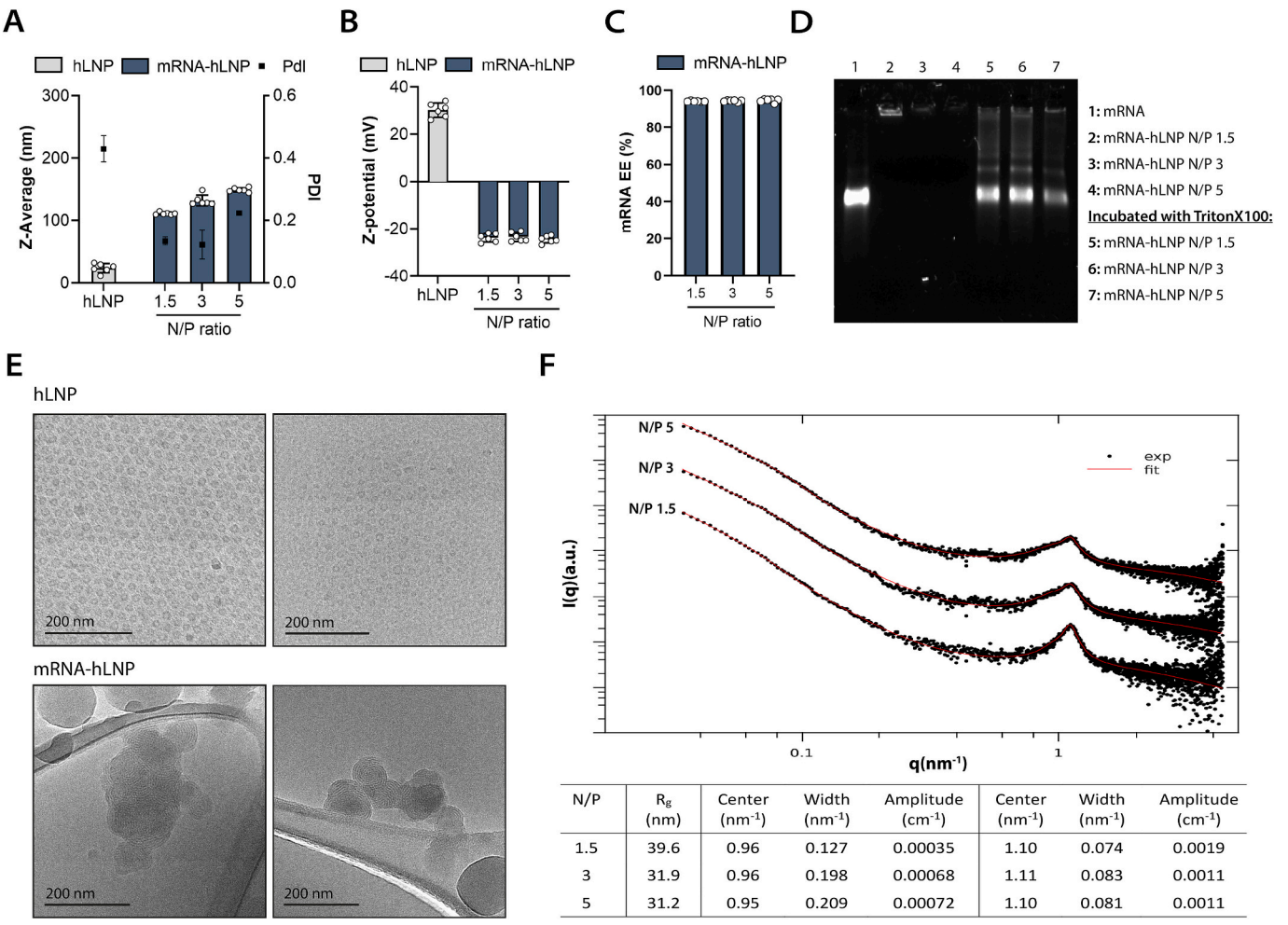

N/P	R_g (nm)	Center (nm^{-1})	Width (nm^{-1})	Amplitude (cm^{-1})	Center (nm^{-1})	Width (nm^{-1})	Amplitude (cm^{-1})
1.5	39.6	0.96	0.127	0.00035	1.10	0.074	0.0019
3	31.9	0.96	0.198	0.00068	1.11	0.083	0.0011
5	31.2	0.95	0.209	0.00072	1.10	0.081	0.0011

Fig. 2. Physicochemical characterization of mRNA-hLNP. (A) Average hydrodynamic diameter, polydispersity index and (B) ζ-potential of mRNA-hLNP at different N/P ratios ($n = 6$ independent replicates). (C) mRNA encapsulation efficiency (EE) determined by RiboGreen® assay. (D) RNA retardation assays to assess the mRNA association efficiency with hLNP. (E) Cryo-TEM images unveiling hLNP morphology and internal structure pre- and post-mRNA complexation at an N/P ratio of 1.5 (additional images are available in supplementary Fig. S1). (F) SAXS profiles of mRNA-hLNP at different N/P ratios with corresponding structural dimensions extracted from the fit.

in the study, resulted in reduced transfection efficacy, underscoring the importance of trehalose in preserving the structural integrity of the lipid membrane (supplementary Fig. S2 and S3). All nanosystems freeze-dried using a mixture of trehalose and mannitol were characterized with a size around 180–200 nm, which was slightly larger than prior to lyophilization process (Fig. 3C). Electrophoretic displacement assays revealed a high preservation of mRNA association with the hLNP, further supported by the preserved morphological integrity of the mRNA-hLNP internal structure (Fig. 3D and F). Measuring the osmotic pressure of nanoparticle suspensions following freeze-drying process is crucial to ensure isotonicity and maintain tissue homeostasis upon injection. Given that biological fluids have an osmolality of approximately 300 mOsmol/kg, the optimal freeze-drying conditions for our mRNA-hLNP involve using 5% mannitol with 1 or 2.5% trehalose, ensuring a suitable balance between particle size and tolerated osmolality (Fig. 3E).

Altogether, these results underscore the efficiency of our innovative lipid-based nanosystem to associate mRNA while enabling long-term stability through lyophilization.

3.3. *Muscle cells are important players for mRNA vaccine delivery*

The role of muscle cells in the delivery pathway of our mRNA-loaded hLNP was initially investigated *in vitro* using both proliferating myoblasts and differentiated myotubes from the C2C12 murine cell line. Regarding myoblasts, mRNA-loaded hLNP tested at different N/P ratios exhibited dose-dependent GFP expression, with higher efficacy observed at lower N/P ratios and achieving up to 76.2% of cells transfected (Fig. 4A and B). No obvious cytotoxicity was observed, further emphasizing the high biocompatibility of mRNA-hLNP (Fig. 4C). These results were also confirmed for lyophilized mRNA-loaded hLNP which displayed slightly lower but still high transfection efficiency on these cells, highlighting the functional integrity of our mRNA-loaded hLNP after lyophilization process (supplementary Fig. S3). In light of the superior transfection efficiency of the mRNA-loaded hLNP at an N/P ratio of 1.5, combined with high cell viability, this condition was selected for further studies. Concerning the myotubes, up to 80.3% of cells expressed GFP, with no overt signs of toxicity observed (Fig. 4D).

The investigation of the intracellular distribution of our mRNA-loaded hLNP was assessed by fluorescent confocal microscopy and revealed a rapid, efficient and time-dependent internalization of the nanosystem with a cytoplasmic accumulation (Fig. 4E). Furthermore, the release of the nucleic acid cargo was studied through the colocalization of the fluorescently labelled-mRNA and -hLNP entities. Confocal images demonstrated an efficient and time-dependent intracellular release of mRNA from the hLNP, as the colocalization of both signals rapidly decreased over time.

Encouraged by these findings, the efficacy of the mRNA-loaded hLNP to transfect matured muscle cells was then investigated in *in vitro* culture

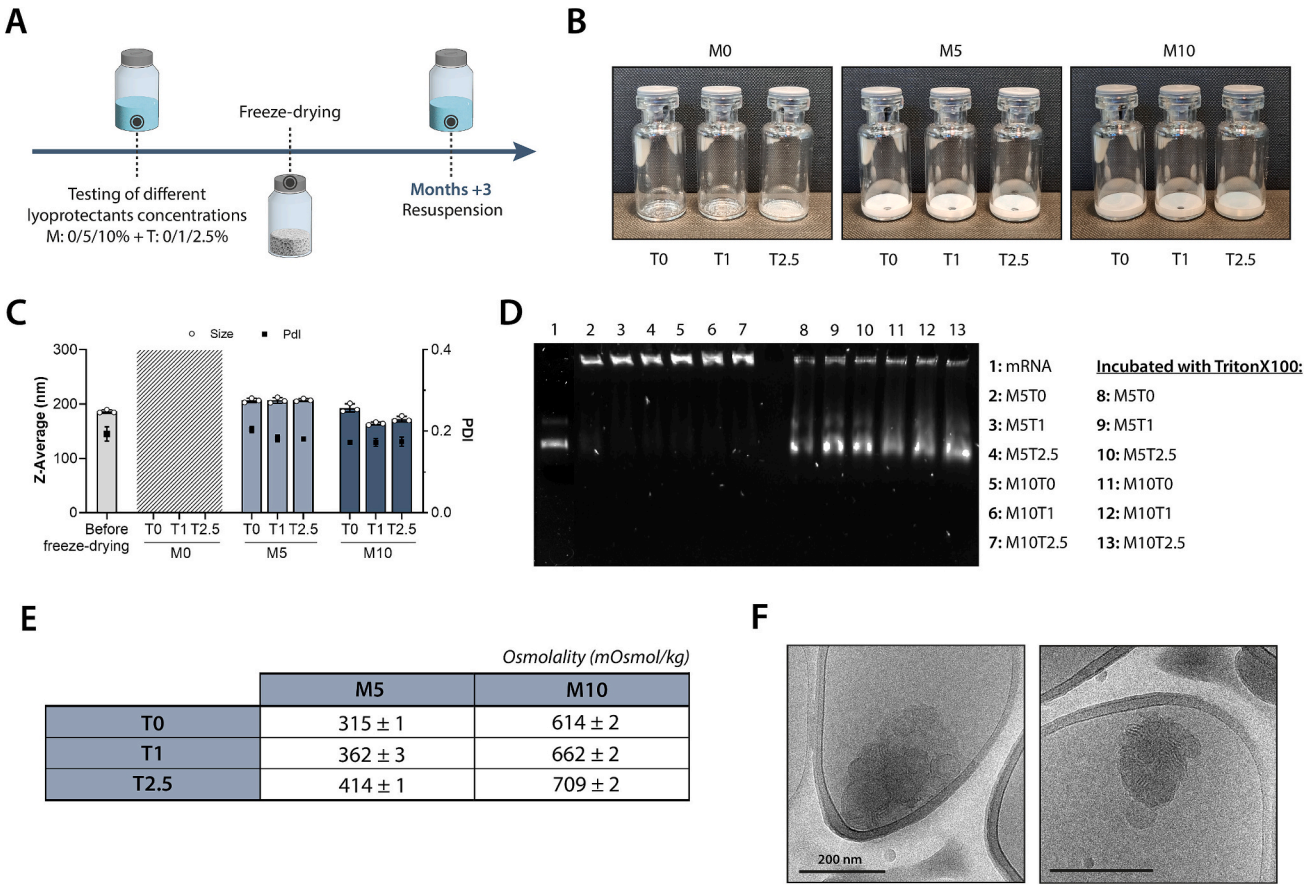

	M5	M10
T0	315 ± 1	614 ± 2
T1	362 ± 3	662 ± 2
T2.5	414 ± 1	709 ± 2

Fig. 3. Freeze-drying process of mRNA-hLNP at varying concentrations of mannitol (M) and trehalose (T). (A) Representative illustration of the freeze-drying process of mRNA-hLNP. (B) Images of the different lyophilized cakes obtained following freeze-drying process. (C) Average hydrodynamic diameter and PDI of the different resuspended lyophilized formulations ($n = 3$). (D) RNA retardation assays to assess the mRNA association efficiency with hLNP following freeze-drying procedure. (E) Osmolality values (mOsmol/kg) of the different formulations (n = 3). (F) Cryo-TEM micrographs of mRNA-hLNP freeze-dried with T1M5.

of explanted muscle fibers. Following *in vitro* culture of explanted muscle fibers, confocal images demonstrated a significant accumulation of the mRNA-hLNP onto the muscle fiber membranes (Fig. 4F). Foremost, efficient transfection of the muscle fibers was achieved, as evidenced by the GFP expression observable at 24 h and sustained up to 72 h post-treatment. Permeabilization of the sample with detergent during immunofluorescence labelling to enhance the GFP signal revealed a homogeneous distribution of GFP protein along the muscle fibers but resulted in the removal of lipid nanoparticles (supplementary Fig. S4).

Different cell types play specialized roles in activating the immune response, with diverse mechanisms being triggered depending on the cell types transfected by mRNA-hLNP. To evaluate functional delivery and determine the transfected cell populations, intramuscular injections of Cre mRNA-loaded hLNP were carried out in the Cre reporter mouse model Ai9-Rosa TdTomato. Upon Cre recombinase expression, the cells of this Cre reporter mouse strain stably express the fluorescent TdTomato protein. First, biodistribution studies were performed to investigate the LNP distribution and protein expression after intramuscular administration. Fluorescence imaging on isolated organs demonstrated that mRNA-hLNP remained highly localized within the injected tibialis anterior (TA) muscle and no obvious accumulation was observed in major organs (liver, kidneys, spleen, lungs, heart and inguinal lymph nodes) compared to other typical LNPs formulations that reach the systemic circulation and accumulate in liver or spleen [12,32] (Fig. 5A). One-week post-administration, the fluorescence signal from the hLNP highly decreased reflecting particles clearance but more interestingly, a high level of protein expression was observed within the TA muscle (Fig. 5A-C). Transversal cross-sections of the injected muscles confirmed robust TdTomato expression, with more than half of the muscle fibers expressing a strong TdTomato signal (Fig. 5D). Notably, mRNA-hLNP signal and TdTomato fluorescence colocalized to restricted areas of the muscle, likely corresponding to the injection site. No signal was observed in adjacent muscles, such as the extensor digitorum longus, which lies lateral and deep into the TA. More interestingly, whole-organ imaging following muscle tissue clearing revealed that transfected fibers expressed TdTomato throughout their entire length (Fig. 5E). This finding suggests that a potential antigen encoded by mRNA can achieve wide expression along the entire muscle fibers.

We next investigated TdTomato expression in specific immune cells within muscles and in secondary lymphoid organs. Confocal images obtained with specific antibodies of dendritic cells or macrophages revealed that none of these cells expressed TdTomato within the muscle tissue. In secondary lymphoid organs, TdTomato expressing cells were absent in the inguinal lymph nodes but some were detected in the spleen (Fig. 5F and supplementary Fig. S5). Immunofluorescence analysis revealed that the rare TdTomato-positive cells detected in the spleen were predominantly macrophages. No $CD11c^{+}TdTomato^{+}$ cells were identified, whereas approximately 47% of $CD64^{+}$ cells expressed TdTomato (supplementary Fig. S5C). Probably, these macrophages were transfected by the mRNA-hLNP in the muscle, or they may have phagocytosed transfected muscle cells.

Taken together, these results highlight the highly efficient transfection of muscle fibers by our mRNA-LNP, with only minor transfection observed in a small subset of macrophages.

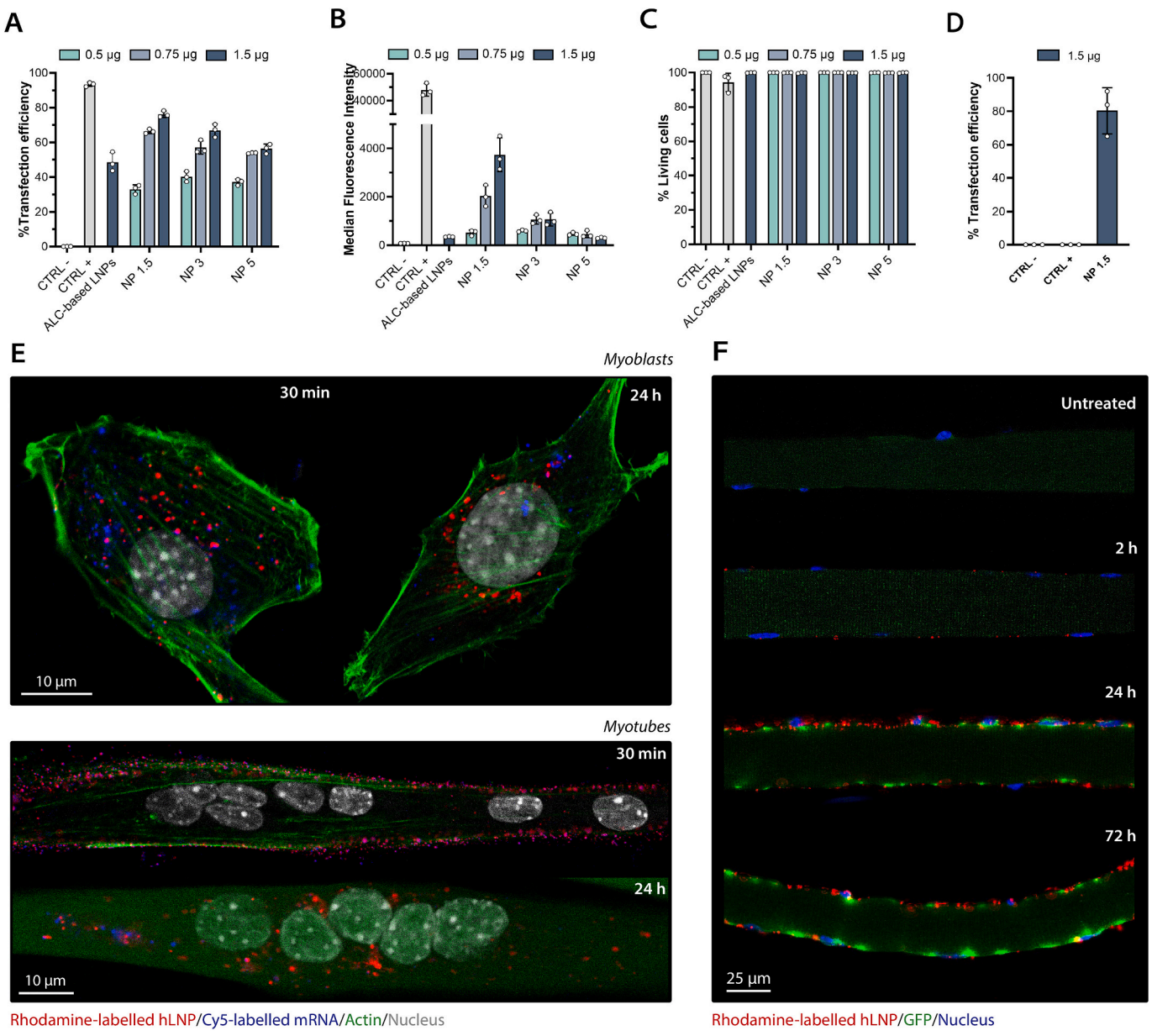

Fig. 4. mRNA uptake, efficacy and affinity of mRNA(GFP)-hLNP for muscle cells *in vitro* and *ex vivo*. (A) Transfection efficiency, (B) median fluorescence intensity (MFI) and (C) cell viability of C2C12 murine muscle myoblasts analyzed by flow cytometry 24 h after mRNA(GFP)-hLNP transfection at varying N/P ratios and mRNA doses ($n = 3$). (D) Transfection efficiency of C2C12 murine differentiated myotubes evaluated by manual counting 24 h after mRNA(GFP)-hLNP transfection at N/P ratio 1.5 (n = 3). (E) Intracellular distribution and mRNA release profile of mRNA(GFP)-hLNP (N/P 1.5) over time in C2C12 murine myoblasts and myotubes, investigated at confocal fluorescence microscopy. Fluorescent signals correspond to: hLNP (red), mRNA (blue), actin filament (green), and nucleus (grey). (F) Distribution and transfection efficiency of mRNA(GFP)-hLNP (N/P 1.5) in explanted murine muscle fibers over time observed at confocal fluorescence microscopy. Fluorescent signals correspond to: hLNP (red), GFP (green), and nucleus (blue).

3.4. Profiling of mRNA vaccine response

To assess the potential of muscle-specific mRNA-hLNP as a vaccine platform, we delivered full-length ovalbumin (OVA) mRNA encapsulated in our hLNP. C57BL/6 J mice received prime (day 0) and boost (day 14) immunizations with either OVA mRNA-hLNP or empty hLNP (Fig. 6A). Antigen-specific IgG antibody titers were measured six days post-injection. A positive control group received a protein-based vaccination regimen based on the subcutaneous OVA protein injection (100 µg) at the tail base, combined with the intraperitoneal injection of 50 µg CD40-specific mAb and 50 mg imiquimod cream (5% Aldara; MEDA) applied on the vaccination site [33]. The OVA mRNA-hLNP vaccination elicited significantly higher anti-OVA IgG titers compared to hLNP alone, and titers were similar to those achieved with the positive control protein-based immunization (Fig. 6B). Notably, analysis of IgG subclasses revealed the presence of anti-OVA IgG2b and IgG2c, as well as IgG1 and IgG3, although the latter were detected at lower levels (supplementary Fig. S6). Furthermore, we observed increased levels of interleukin (IL)-6, IL-12p70, IFN-γ, and granulocyte-macrophage colony-stimulating factor (GM-CSF) in the plasma of vaccinated mice (Fig. 6C). Altogether, the mRNA-hLNP formulation induced a pro-inflammatory response similar to that triggered by the protein-based vaccine. These soluble mediators contribute to the activation of APCs, able to promote a Th1-skewed polarization of $CD4^+$ T cells, which supports IgG isotype switching. This outcome demonstrates the mRNA-hLNP vaccine's capability to induce a robust antigen-specific humoral

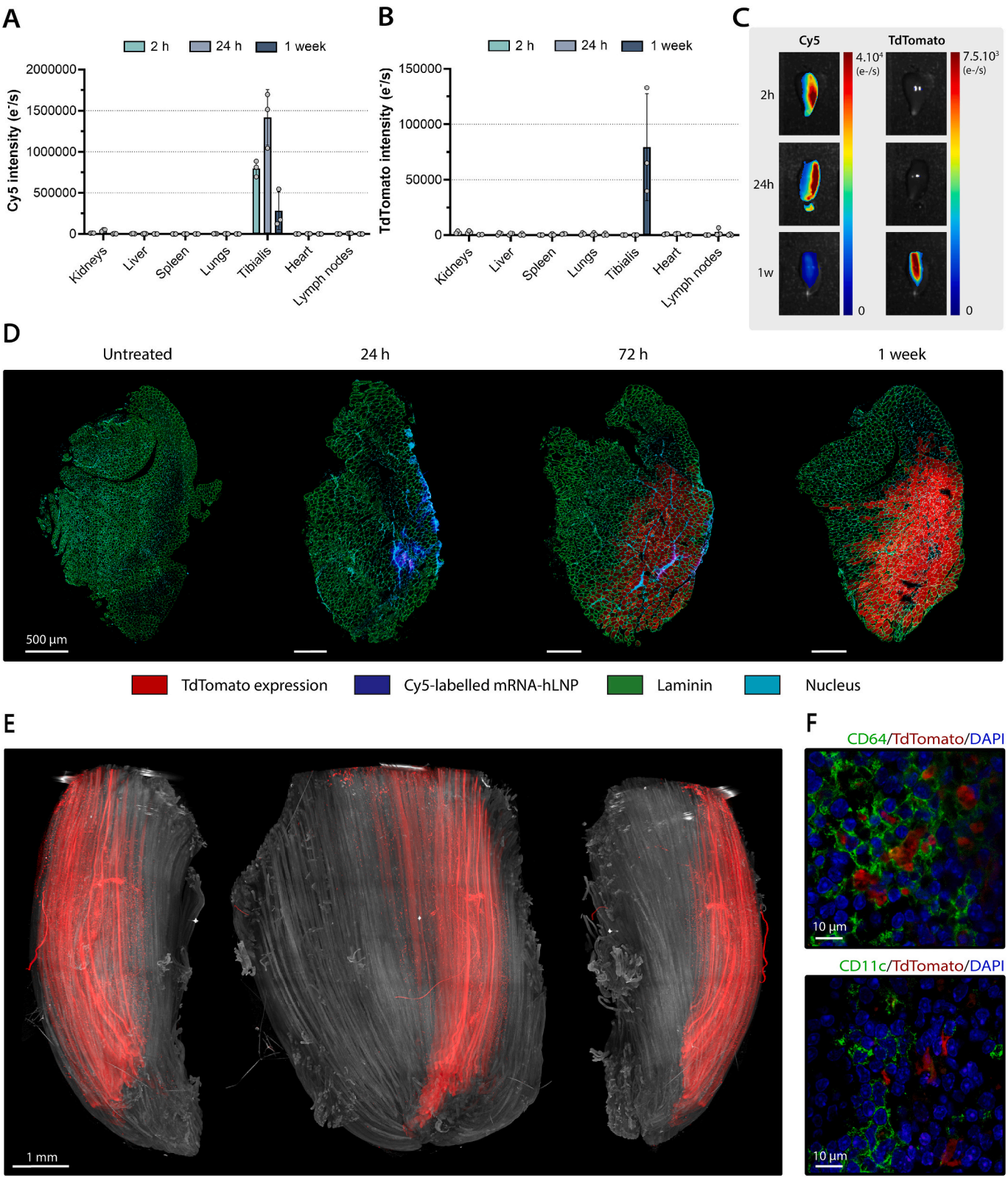

Fig. 5. Tissue biodistribution and transfection efficiency of mRNA(Cre)-hLNP following i.m. administration (0.25 mg/kg) in the Ai9-Rosa TdTomato reporter mouse model. (A) Semi-quantification of mRNA(Cre)-hLNP and (B) TdTomato protein expression in various organs over time following i.m. administration into the tibialis anterior muscle ($n = 3$). (C) Representative *ex vivo* images of tibialis anterior muscles over time following i.m. administration (D) Transversal cross-section of the injected tibialis anterior observed at confocal fluorescence microscopy (n = 3). Fluorescent signals correspond to: mRNA(Cre)-hLNP (blue), TdTomato (red), laminin (green), and nucleus (light blue). (E) Whole-organ visualization of TdTomato protein expression in the injected tibialis anterior (1-week post-administration), investigated using light sheet microscopy after tissue clearing ($n = 1$). (F) Characterization of splenic TdTomato+ cells after mRNA(Cre)-hLNP i.m. administration. Fluorescent signals correspond to: monocytes/macrophages (CD64, green), dendritic cells (CD11c, green), TdTomato (red), and nucleus (DAPI). (For interpretation of the references to color in this figure legend, the reader is referred to the web version of this article.)

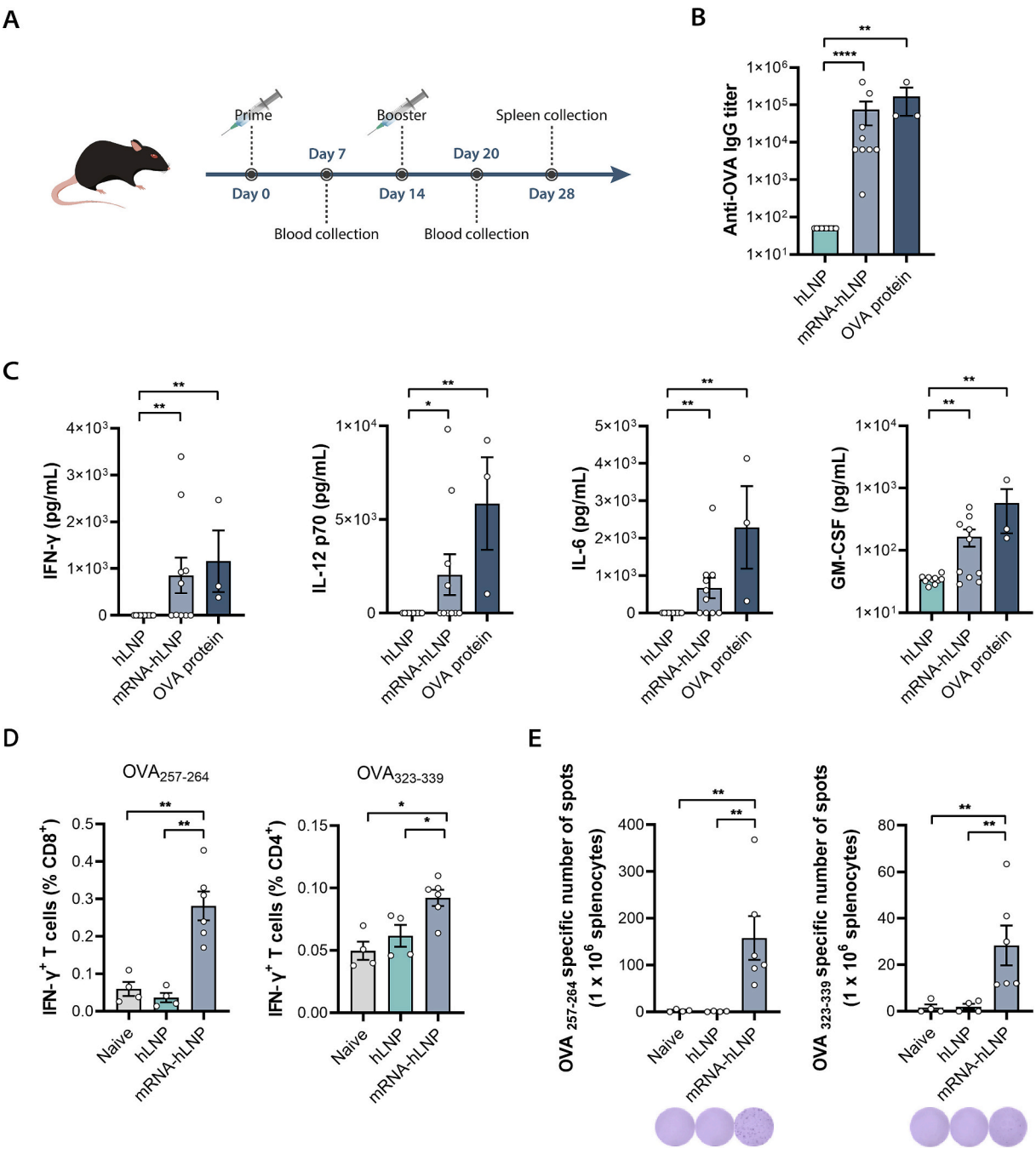

Fig. 6. Cellular and humoral immune responses after intramuscular mRNA(OVA)-hLNP vaccination. (A) Representative timeline for vaccination and sample collection. (B) anti-OVA IgG titer in the serum of mice 20 days after immunization with unloaded hLNP, mRNA(OVA)-hLNP vaccine, or OVA protein-based vaccine. (C) Cytokine quantification in the serum of the same mice. (D) Flow cytometry analysis of IFN-γ producing $CD8^+$ (left panel) and $CD4^+$ T cells (right panel) from mouse splenocytes cultured with $OVA_{257–264}$ or $OVA_{323–339}$ peptides in the presence of brefeldin A (n = 4–6). (E) OVA-specific IFN-γ ELISPOT from mouse splenocytes re-stimulated with $OVA_{257–264}$ or $OVA_{323–339}$ peptides (n = 4–6). The histogram displays the number of specific IFN-γ spots, normalized by subtracting background spots to unrelated peptides. Below each column a representative ELISPOT well is displayed.

response. We then conducted *ex vivo* stimulation of splenocytes from both vaccinated and unvaccinated mice using MHC-I ($OVA_{257–264}$) and MHC-II OVA ($OVA_{323–329}$) epitopes, respectively. We assessed immune responses using flow cytometry, evaluating the percentage of IFN-γ-producing $CD8^+$ or $CD4^+$ T cells among stimulated splenocytes. Following $OVA_{257–264}$ peptide *in vitro* stimulation, mice vaccinated with mRNA-hLNP showed a significant increase in IFN-γ^+ cytotoxic T lymphocytes (CTLs) compared to controls (Fig. 6D, left panel; supplementary Fig. S7). We also observed a Th1-restricted immune response following *in vitro* stimulation with $OVA_{323–329}$ peptide, although it was less pronounced compared to the CTL response (Fig. 6D, right panel). To validate our findings, an ELISPOT assay confirmed that the OVA mRNA-hLNP vaccine elicited a robust adaptive cellular immune response, involving both $CD4^+$ and $CD8^+$ T cells, with a pronounced cytotoxic immune response against ovalbumin (Fig. 6E). Collectively, these findings suggest that mRNA-hLNP can serve as an effective mRNA vaccine platform by eliciting both arms of adaptive immunity. Although the $CD4^+$ T cell response is less robust than the $CD8^+$ T cell response, the expanded Th1-based cellular immunity remains functional, as evidenced by its ability to facilitate isotype switching and the production of specific

anti-OVA IgG antibodies.

4. Discussion

The recent development of mRNA-vaccines highlighted the great increasing potential of this technology to expand the landscape of modern vaccine development.

In this work, we described the development of an innovative hybrid lipid-polymer nanoparticles formulation engineered for nucleic acid delivery. Notably, this PEG-free formulation offers a significant advantage and tolerability, as PEG moiety is at the center of ongoing debate regarding the "PEG-dilemma" and is suspected to be linked to rare cases of anaphylactic reactions following COVID-19 mRNA vaccination [34,35]. The combination of permanently charged cationic lipid and pH-responsive cationic lipid (associated with its cleavable structure) yields complementary advantages, conferring high colloidal stability while promoting enhanced cellular uptake and fostering endosomal escape and cytosolic nucleic acid release [36–38]. This tailored composition provides a highly efficient nanosystem for mRNA delivery, combining controlled particle size, favorable properties to ensure cellular interaction and protection of the nucleic acid cargo. Furthermore, this nanosystem demonstrates high long-term colloidal stability following freeze-drying process. Following storage at 4 °C for a few months, freeze-dried formulations demonstrated, after resuspension, preserved structural architecture and integrity, with closely similar physicochemical properties and reliable performance over time. These suitable properties confer practical advantages, enabling the development of a broader accessibility mRNA-based LNP vaccine with prolonged shelf-life and improve ease of storage and distribution [39].

The first seminal studies on mRNA-based vaccines emphasized that achieving robust transfection efficiency in APCs is a critical determinant to provide a successful mRNA vaccine [11,40,41]. Hassett et al. investigated the cellular trafficking of their mRNA-LNPs and demonstrated mRNA expression in infiltrating immune cells in both rodents and non-human primates following intramuscular administration, with no mRNA expression in muscle fibers [11]. Buckley et al. also demonstrated a rapid trafficking of their mRNA-LNP to different draining lymph nodes after i.m. injection in non-human primates, with APCs primarily responsible for LNP uptake and mRNA translation [42]. It is noteworthy that Takanashi et al. reported a stronger immune response in mice immunized with an LNP formulation displaying comparable transfection efficiency in muscle tissue, but enhanced protein expression in secondary lymphoid organs [43]. Conversely, our mRNA-hLNP demonstrated a pronounced affinity for muscle cells, as evidenced by high levels of protein expression in muscle fibers following intramuscular injection, while APCs exhibited only negligible levels of transfection.

Building on its limited off-target activity, we investigated the vaccinal potential of our mRNA-hLNP formulation. Indeed, skeletal muscle is not only a biomechanical organ but also a critical regulator of immunometabolism. It synthesizes glutamine, a vital non-essential amino acid that supports the energy needs of rapidly dividing immune cells such as lymphocytes and macrophages. This enables these cells to effectively perform critical functions like phagocytosis, antigen presentation, and cytokine synthesis [44]. In addition to glutamine, skeletal muscle secretes myokines, including interleukin-6 (IL-6), which modulates immune responses to facilitate tissue healing, and control inflammation [45]. In line with this observation, we detected a systemic pro-inflammatory condition characterized by elevated levels of IL-6 and GM-CSF that can affect myelopoiesis and local immune activation by promoting the generation of APCs. Furthermore, muscle cells release interleukin-15 (IL-15), which attracts precursor T cells to the muscle environment. This helps to protect these cells from exhaustion and supports sustained immune responses. Finally, muscle-derived chemokines can recruit various immune cells, including neutrophils, macrophages, and lymphocytes, further enhancing immune function [46].

Transfection of muscle cells is pivotal in initiating adaptive immune responses by establishing a source of antigen and by inducing immunogenic cell death and antigen release into the extracellular space, supporting recruitment and activation of antigen-presenting cells (APCs) [47]. Myeloid cells here engulf antigen and apoptotic cells to trigger adaptive immune responses in peripheral lymphoid organs [48]. In addition, muscle resident APCs can be directly transfected with antigen-coding mRNA, allowing them to present antigen fragments on their surface *via* both MHC I and MHC II molecules [48]. Our advanced nanoparticles effectively activate adaptive immunity without requiring specialized adjuvants, owing to their engineered formulation that replicates key features of viral infections [49]. Indeed, we evaluated a systemic increase of Th1-polarizing cytokines such as IL-12p70, and IFN-γ that are the two pillars of the activation of Th1 CD4+ T cells. Our results demonstrated significantly stronger CD8+ T cell activation compared to $CD4^+$ T cell responses. Nonetheless, Th1 specific immunity supports IgG isotype switching, thereby mirroring the effects achieved with protein-based vaccines when paired with strong adjuvants like imiquimod. In summary, intramuscular mRNA-hLNP delivery has demonstrated remarkable efficacy in eliciting antigen-specific systemic immune responses. In the future, a further improvement could be testing the immune responses evoked by the vaccine towards a cancer-associated neoantigen.

5. Conclusion

In this work, the successful development of a PEG- and cholesterol-free hybrid lipid-polymer nanosystem enabling efficient mRNA association and delivery is reported. Moreover, this hLNP formulation displayed remarkable long-term stability under standard storage conditions following the freeze-drying process, preserving its physicochemical integrity and functional efficiency over time. *In vitro* studies performed on murine muscle cell line, in both proliferating and differentiated states, confirmed the high transfection capacity of this nanosystem, leading to robust mRNA expression while maintaining excellent cell viability. The biodistribution and cellular engagement analyses further support the involvement of muscle tissue as an active site contributing to antigen expression and subsequent immune activation.

These findings established an efficient and stable mRNA delivery platform, offering valuable insights into the important role of muscle cells in mRNA vaccine efficacy as antigen-producing reservoirs and paving the way for the next generation of safe and effective LNP-based vaccines.

CRediT authorship contribution statement

Mathieu Repellin: Writing – review & editing, Writing – original draft, Methodology, Investigation, Conceptualization. **Stefano Ugel:** Writing – review & editing, Writing – original draft, Funding acquisition, Conceptualization. **Francesco De Sanctis:** Writing – review & editing, Writing – original draft, Funding acquisition, Conceptualization. **Laurent Coudert:** Investigation, Data curation. **Tian Wang:** Investigation, Data curation. **Cristina Anselmi:** Investigation, Data curation. **Valentina Andretto:** Writing – review & editing, Investigation, Data curation, Conceptualization. **Isabella Scionti:** Writing – review & editing, Methodology, Investigation, Data curation, Conceptualization. **Joris Dimastromatteo:** Investigation, Data curation. **Jacqueline Sidi-Boumedine:** Investigation, Data curation. **Julien Carras:** Investigation, Data curation. **Pierre-Yves Dugas:** Methodology, Investigation, Data curation. **Fabrice Brunel:** Writing – review & editing, Methodology, Investigation, Data curation, Conceptualization. **Manuela Malatesta:** Writing – review & editing, Funding acquisition, Conceptualization. **David Kryza:** Methodology, Conceptualization. **Laurent Schaeffer:** Writing – review & editing, Supervision, Funding acquisition, Conceptualization. **Arnaud Jacquier:** Writing – review & editing, Supervision, Investigation, Conceptualization. **Giovanna Lollo:** Writing – review & editing, Writing – original draft, Supervision, Funding acquisition,

Conceptualization.

Acknowledgments

The authors acknowledge the contribution of SFR-Santé Lyon Est (UAR3453 CNRS, US7 Inserm, UCBL) facility: CIQLE (a LyMIC member), especially Bruno Chapuis for his knowledge and help on tissue clearing and light sheet microscopy acquisition.

The authors thank the European Synchrotron Radiation Facility (ESRF) for provision of synchrotron radiation facilities under proposal number SC-5519, and especially Manna Gouranga for assistance and support in using beamline ID02.

The authors acknowledge the Innobiovir platform for providing access to freeze-drying equipment.

This work was supported by Giovanna Lollo and Laurent Schaeffer grants of the Technology Transfer Accelerator Office Lyon-Saint-Etienne Pulsalys (Project "RESOLVE") and the AFM-Telethon (Project "Nano-Myo", application number 25161). This work was supported by Laurent Schaeffer grant of the ANR (Project MUSCLE; ANR-24-PEBI-0003) within the framework of the PEPR BBTI ("Biothérapies et Bioproduction de Thérapies Innovantes") program. This research project was also supported by Giovanna Lollo grant of the ANR (Project LNP@HiRes; ANR-24-29CE-5467-01). This project has received funding from the European Union's Horizon 2020 Research and Innovation Programme under the Marie Skłodowska-Curie grant agreement No. 754345.

This work was jointly supported by Stefano Ugel grants of the Fondazione Italiana per la Ricerca sul Cancro (AIRC) (MFAG project: 21509; Bridge project: 28730), Fondazione Italiana Sclerosi Multipla (AISM/FISM) (project reference: 2024/R-Single/035, CUP: B37G25000050007), and PNRR programs of the Italian MUR (Project "National Center for Gene Therapy and Drugs based on RNA Technology", application code CN00000041, Mission 4, Component 2 Investment 1.4, funded from the European Union – Next Generation EU, MUR Directorial Decree No. 1035 of 17 June 2022, CUP B33C22000630001), and Francesco De Sanctis grant by PRIN programs of the Italian Ministry of Education, University, and Research (CUP: B39J22001200001). Tian Wang is supported by AIRC fellowship for Italy (Call 2024).

Appendix A. Supplementary data

Supplementary data to this article can be found online at https://doi.org/10.1016/j.jconrel.2026.115128.

Data availability

Data will be made available on request.

References

[1] A. Akinc, et al., The Onpattro story and the clinical translation of nanomedicines containing nucleic acid-based drugs, Nat. Nanotechnol. 14 (2019) 1084–1087.
[2] L.R. Baden, et al., Efficacy and safety of the mRNA-1273 SARS-CoV-2 vaccine, N. Engl. J. Med. 384 (2021) 403–416.
[3] U. Sahin, et al., COVID-19 vaccine BNT162b1 elicits human antibody and TH1 T cell responses, Nature 586 (2020) 594–599.
[4] Y. Shi, M. Shi, Y. Wang, J. You, Progress and prospects of mRNA-based drugs in pre-clinical and clinical applications, Signal Transduct. Target. Ther. 9 (2024) 322.
[5] B. Bollman, et al., An optimized messenger RNA vaccine candidate protects non-human primates from Zika virus infection, NPJ Vaccines 8 (2023) 58.
[6] E. Wilson, et al., Efficacy and safety of an mRNA-based RSV PreF vaccine in older adults, N. Engl. J. Med. 389 (2023) 2233–2244.
[7] I. Dinulovic, R. Furrer, C. Handschin, Plasticity of the muscle stem cell microenvironment, Adv. Exp. Med. Biol. 1041 (2017) 141–169.
[8] V.R. Kedlian, et al., Human skeletal muscle aging atlas, Nat. Aging 4 (2024) 727–744.
[9] K. Kubara, et al., Lymph node macrophages drive innate immune responses to enhance the anti-tumor efficacy of mRNA vaccines, Mol. Ther. J. Am. Soc. Gene Ther. 32 (2024) 704–721.
[10] M. Gomi, et al., Delivering mRNA to secondary lymphoid tissues by phosphatidylserine-loaded lipid nanoparticles, Adv. Healthc. Mater. 12 (2023) 2202528.
[11] K.J. Hassett, et al., mRNA vaccine trafficking and resulting protein expression after intramuscular administration, Mol. Ther. Nucleic Acids 35 (2024) 102083.
[12] J. Chen, et al., Combinatorial design of ionizable lipid nanoparticles for muscle-selective mRNA delivery with minimized off-target effects, Proc. Natl. Acad. Sci. USA 120 (2023) e2309472120.
[13] A. Marks, et al., mRNA vaccine immunity is enhanced by hepatocyte detargeting and not dependent on dendritic cell expression, Nat. Biotechnol. (2026) 1–15.
[14] M. Marino, F. Scuderi, C. Provenzano, E. Bartoccioni, Skeletal muscle cells: from local inflammatory response to active immunity, Gene Ther. 18 (2011) 109–116.
[15] A.M. Afzali, T. Müntefering, H. Wiendl, S.G. Meuth, T. Ruck, Skeletal muscle cells actively shape (auto)immune responses, Autoimmun. Rev. 17 (2018) 518–529.
[16] A.O. Mann, et al., IL-17A-producing γδT cells promote muscle regeneration in a microbiota-dependent manner, J. Exp. Med. 219 (2022) e20211504.
[17] V. Andretto, et al., Hybrid core-shell particles for mRNA systemic delivery, J. Control. Release 353 (2023) 1037–1049.
[18] G. Lollo, et al., Nanoparticules pour la liberation d'acides nucleiques, WO2023099722A1, 2023.
[19] K. Su, et al., Reformulating lipid nanoparticles for organ-targeted mRNA accumulation and translation, Nat. Commun. 15 (2024) 5659.
[20] M. Kawaguchi, et al., Effect of cholesterol content of lipid composition in mRNA-LNPs on the protein expression in the injected site and liver after local administration in mice, J. Pharm. Sci. 112 (2023) 1401–1410.
[21] K. Tainaka, et al., Chemical landscape for tissue clearing based on hydrophilic reagents, Cell Rep. 24 (2018) 2196–2210.e9.
[22] J.G. Facciponte, et al., Tumor endothelial marker 1-specific DNA vaccination targets tumor vasculature, J. Clin. Invest. 124 (2014).
[23] S. Ugel, et al., Autoimmune B-cell lymphopenia after successful adoptive therapy with telomerase-specific T lymphocytes, Blood 115 (2010) 1374–1384.
[24] E. Mylona, K.A. Jones, S.T. Mills, G.K. Pavlath, CD44 regulates myoblast migration and differentiation, J. Cell. Physiol. 209 (2006) 314–321.
[25] C.D. Siewert, et al., Hybrid biopolymer and lipid nanoparticles with improved transfection efficacy for mRNA, Cells 9 (2020) 2034.
[26] J.A. Kulkarni, et al., On the formation and morphology of lipid nanoparticles containing Ionizable cationic lipids and siRNA, ACS Nano 12 (2018) 4787–4795.
[27] A. Witkowska, L.P. Heinz, H. Grubmüller, R. Jahn, Tight docking of membranes before fusion represents a metastable state with unique properties, Nat. Commun. 12 (2021) 3606.
[28] G. Vancuylenberg, A. Sadeghpour, A.I.I. Tyler, M. Rappolt, Planar confined water organisation in lipid bilayer stacks of phosphatidylcholine and phosphatidylethanolamine, Soft Matter 19 (2023) 5179–5192.
[29] D.J.A. Crommelin, T.J. Anchordoquy, D.B. Volkin, W. Jiskoot, E. Mastrobattista, Addressing the cold reality of mRNA vaccine stability, J. Pharm. Sci. 110 (2021) 997–1001.
[30] C. Chen, D. Han, C. Cai, X. Tang, An overview of liposome lyophilization and its future potential, J. Control. Release Off. J. Control. Release Soc. 142 (2010) 299–311.
[31] S. Meulewaeter, et al., Continuous freeze-drying of messenger RNA lipid nanoparticles enables storage at higher temperatures, J. Control. Release 357 (2023) 149–160.
[32] M.J. Carrasco, et al., Ionization and structural properties of mRNA lipid nanoparticles influence expression in intramuscular and intravascular administration, Commun. Biol. 4 (2021) 956.
[33] Y. Hailemichael, et al., Persistent antigen at vaccination sites induces tumor-specific $CD8^+$ T cell sequestration, dysfunction and deletion, Nat. Med. 19 (2013) 465–472.
[34] C.A. Stone, et al., Immediate hypersensitivity to polyethylene glycols and polysorbates: more common than we have recognized, J Allergy Clin Immunol Pract 7 (2019) 1533–1540.e8.
[35] M.C. Castells, E.J. Phillips, Maintaining safety with SARS-CoV-2 vaccines, N. Engl. J. Med. 384 (2021) 643–649.
[36] A.K. Dey, et al., Tuning the Immunostimulation properties of cationic lipid Nanocarriers for nucleic acid delivery, Front. Immunol. 12 (2021).
[37] G.S. Naidu, et al., A combinatorial library of lipid nanoparticles for cell type-specific mRNA delivery, Adv. Sci. Weinh. Baden-Wurtt. Ger. 10 (2023) e2301929.
[38] R. Oyama, et al., An Ionizable lipid material with a vitamin E scaffold as an mRNA vaccine platform for efficient cytotoxic T cell responses, ACS Nano 17 (2023) 18758–18774.
[39] E. Oude Blenke, et al., The storage and in-use stability of mRNA vaccines and therapeutics: not a cold case, J. Pharm. Sci. 112 (2023) 386–403.
[40] B. Clemente, et al., Straight to the point: targeted mRNA-delivery to immune cells for improved vaccine design, Front. Immunol. 14 (2023) 1294929.
[41] K.J. Hassett, et al., Optimization of lipid nanoparticles for intramuscular administration of mRNA vaccines, Mol. Ther. Nucleic Acids 15 (2019) 1–11.
[42] M. Buckley, et al., Visualizing lipid nanoparticle trafficking for mRNA vaccine delivery in non-human primates, Mol. Ther. J. Am. Soc. Gene Ther. 33 (2025) 1105–1117.
[43] A. Takanashi, C.W. Pouton, H. Al-Wassiti, Delivery and expression of mRNA in the secondary lymphoid organs drive immune responses to lipid nanoparticle-mRNA vaccines after intramuscular injection, Mol. Pharm. 20 (2023) 3876–3885.
[44] V. Cruzat, M. Macedo Rogero, K. Noel Keane, R. Curi, P. Newsholme, Glutamine: metabolism and immune function, supplementation and clinical translation, Nutrients 10 (2018) 1564.

[45] M.A. Febbraio, B.K. Pedersen, Muscle-derived interleukin-6: mechanisms for activation and possible biological roles, FASEB J. 16 (2002) 1335–1347.
[46] J. Wu, et al., Skeletal muscle antagonizes antiviral CD8+ T cell exhaustion, Sci. Adv. 6 (2020) eaba3458.
[47] Y.-Y. Lin, et al., Skeletal muscle is an antigen reservoir in integrase-defective lentiviral vector-induced long-term immunity, Mol. Ther. Methods Clin. Dev. 17 (2020) 532–544.
[48] N. Chaudhary, D. Weissman, K.A. Whitehead, mRNA vaccines for infectious diseases: principles, delivery and clinical translation, Nat. Rev. Drug Discov. 20 (2021) 817–838.
[49] T.G. Dacoba, A. Olivera, D. Torres, J. Crecente-Campo, M.J. Alonso, Modulating the immune system through nanotechnology, Semin. Immunol. 34 (2017) 78–102.